



HAL
open science

Numerical Analysis of the Atmospheric Boundary-Layer Turbulence Influence on Microscale Transport of Pollutant in an Idealized Urban Environment

Tim Nagel, Robert Schoetter, Valéry Masson, Christine Lac, Bertrand
Carissimo

► **To cite this version:**

Tim Nagel, Robert Schoetter, Valéry Masson, Christine Lac, Bertrand Carissimo. Numerical Analysis of the Atmospheric Boundary-Layer Turbulence Influence on Microscale Transport of Pollutant in an Idealized Urban Environment. *Boundary-Layer Meteorology*, In press, 10.1007/s10546-022-00697-7. meteo-03625286

HAL Id: meteo-03625286

<https://meteofrance.hal.science/meteo-03625286>

Submitted on 30 Mar 2022

HAL is a multi-disciplinary open access archive for the deposit and dissemination of scientific research documents, whether they are published or not. The documents may come from teaching and research institutions in France or abroad, or from public or private research centers.

L'archive ouverte pluridisciplinaire **HAL**, est destinée au dépôt et à la diffusion de documents scientifiques de niveau recherche, publiés ou non, émanant des établissements d'enseignement et de recherche français ou étrangers, des laboratoires publics ou privés.

1 **Numerical Analysis of the Atmospheric**
2 **Boundary-Layer Turbulence Influence on Microscale**
3 **Transport of Pollutant in an Idealized Urban**
4 **Environment**

5 **Tim Nagel · Robert Schoetter · Valéry**
6 **Masson · Christine Lac · Bertrand**
7 **Carissimo**

8
9 Received: DD Month YEAR / Accepted: DD Month YEAR

10 **Abstract** The mesoscale atmospheric model Meso-NH is used to investigate
11 the influence of the mesoscale atmospheric turbulence on the mean flow, tur-
12 bulence, and pollutant dispersion in an idealized urban-like environment, the
13 array of containers investigated during the Mock Urban Setting Test field
14 experiment. First, large-eddy simulations are performed as in typical compu-
15 tational fluid dynamics-like configurations, i.e., without accounting for the at-
16 mospheric boundary-layer (ABL) turbulence on scales larger than the building
17 scale. Second, in a multiscale configuration, turbulence of all scales prevailing
18 in the ABL is accounted for by using the grid-nesting approach to downscale
19 from the meso- to the microscale. The building-like obstacles are represented
20 using the immersed boundary method and a new turbulence recycling method
21 is used to enhance the turbulence transition between two nested domains.

22 Upstream of the container array, flow characteristics such as wind speed,
23 direction and turbulence kinetic energy are well reproduced with the mul-
24 tiscale configuration, showing the efficiency of the grid-nesting approach in
25 combination with turbulence recycling for downscaling from the meso- to
26 the microscale. Only the multiscale configuration is able to reproduce the
27 mesoscale turbulent structures crossing the container array. The accuracy of
28 the numerical results is evaluated for wind speed, wind direction, and pollu-
29 tant concentration. The microscale numerical simulation of wind speed and
30 pollutant dispersion in an urban-like environment benefits from taking into
31 account the ABL turbulence. However, this benefit is significantly less im-

T. Nagel, R. Schoetter, V. Masson, C. Lac
Centre National de Recherches Météorologiques (Météo-France), 42 avenue Gaspard Coriolis
31057 Toulouse, France.
E-mail: tim.nagel@meteo.fr; robert.schoetter@meteo.fr

B. Carissimo
CEREA, Teaching and Research Center in Atmospheric Environment (ENPC/EDF R&D),
6 Quai Watier 78400 CHATOU Cedex, France.

portant than what is described in the literature for the Oklahoma City Joint Urban 2003 real case. The present study highlights that pollutant dispersion simulation improvement when accounting for ABL turbulence is dependent on the specific configuration of the city.

Keywords Idealized urban environment · Immersed boundary method · Large-eddy simulations · Meso–Microscale interaction · Pollutant transport

1 Introduction

Cities have an impact on the atmospheric boundary-layer (ABL) by modifying its dynamical and thermodynamical structure. They also release a significant amount of pollutant into the atmosphere. The concentration and the residence time of pollutants in cities are strongly influenced by their geometrical complexity. High values of pollutant concentration and residence time result in environmental and health issues. According to the World Health Organization, air pollution caused 4.2 million premature deaths worldwide in 2016¹. Air quality has therefore become a point of particular interest for inhabitants and policy makers.

The precise quantification of atmospheric flows, pollutant transport, and dispersion in cities is a major modelling challenge (Dauxois et al. 2021). To accurately resolve atmospheric flows and pollutant dispersion in cities it is necessary to account for small-scale fluid dynamical and radiative processes over a complex and heterogeneous terrain including buildings of different dimensions, shapes and materials, streets of various spacing, trees in the streets, parks, and potentially water (river and ponds).

Computational fluid dynamics (CFD) is a very convenient and widely used tool for urban air pollution studies. Reviews by Tominaga and Stathopoulos (2013) or Blocken (2015) show the variety of CFD models available [with turbulence closure from Reynolds-averaged Navier–Stokes (RANS) to large-eddy simulations (LESs)] and some of their applications (from pedestrian comfort to air quality studies). The main advantage of CFD models is their ability to deal with very fine resolution and to resolve complex geometries. With the increase of computational power, CFD models have been applied to areas as large as a part of a city (the downtown of Oklahoma City, for instance, as in García-Sánchez et al. 2018). However, despite recent improvements (García-Sánchez and Gorlé 2018; García-Sánchez et al. 2018), the CFD models’ boundary conditions do not represent the inherent variability of the real ABL. This issue is considered as one of the CFD models’ bottlenecks (Dauxois et al. 2021).

Numerically reproducing atmospheric flow and pollutant dispersion in the urban environment can also be done through multiscale numerical weather prediction (NWP) models such as the Weather Research and Forecasting (WRF, Skamarock et al. 2008) or Meso-NH (where NH means non-hydrostatic, Lac

¹ [https://www.who.int/news-room/fact-sheets/detail/ambient-\(outdoor\)-air-quality-and-health](https://www.who.int/news-room/fact-sheets/detail/ambient-(outdoor)-air-quality-and-health)

72 et al. 2018). Advances in computational resources allow performance of mi-
73 croscale simulations of the ABL at LES resolutions (e.g., Couvreux et al.
74 2020). Provided that meteorological variables are correctly downscaled from
75 mesoscale to microscale resolutions, e.g., using a grid-nesting approach, mul-
76 tiscale NWP models appear as a suitable tool to study the effect of ABL
77 turbulence on the microscale atmospheric flow and pollutant dispersion in an
78 urban environment. A major issue lies in the terrain-following vertical coordi-
79 nate system used in numerous NWP codes. When performing high-resolution
80 simulations over complex terrain, numerical errors arise because of the grid
81 distortion (Zängl et al. 2004). By definition, there is no steeper slope than a
82 vertical building facade. This issue can be overcome thanks to another numeri-
83 cal approach, the immersed boundary method (IBM), which is compatible
84 with NWP models such as WRF (Lundquist et al. 2010, 2012) or Meso-NH
85 (MNH-IBM, Auguste et al. 2019). Recently, Wiersema et al. (2020) performed
86 mesoscale to microscale simulations of the Joint Urban 2003 (JU2003) field
87 campaign in Oklahoma City (Allwine et al. 2004; Allwine and Flaherty 2006)
88 with WRF using the IBM to represent the buildings. They have shown that
89 the pollutant dispersion is better simulated when using a multiscale NWP
90 model rather than a CFD-like model with idealized boundary conditions and
91 a limited domain vertical extent. The study of Wiersema et al. (2020) is based
92 on a real city experimental dataset. The complexity of this real city may gener-
93 ate difficulties in distinguishing between the general impact of buildings and
94 other phenomena like channelling, local recirculation, or pollutant trapping
95 due to a specific configuration of the city (Milliez and Carissimo 2007). Real
96 cases can be simplified while keeping their main advantage, which is the re-
97 alistic meteorological conditions. This is done through field experiments with
98 an idealized city with regular array of rectangular obstacles, such as the Mock
99 Urban Setting Test experiment (MUST, Biltoft 2001; Yee and Biltoft 2004).

100 In the present study, MNH-IBM is used to investigate the influence of
101 the mesoscale atmospheric turbulence on the mean flow, the turbulence, and
102 the pollutant dispersion in the MUST idealized urban-like environment. The
103 influence of a limited vertical extent, which is usually used in CFD simula-
104 tions (Blocken 2015), is also investigated. Three configurations are studied:
105 two CFD-like configurations, with and without limited vertical extent, where
106 a velocity profile is prescribed at the boundaries and a multiscale configura-
107 tion, where the large-scale atmospheric turbulence prevailing in the ABL is
108 accounted for, thanks to grid-nested domains with increasing horizontal reso-
109 lution. A new turbulence recycling method is also introduced to enhance the
110 scale transition of the ABL turbulence.

111 Below, the model is presented in Sect. 2, the MUST experiment and the
112 numerical configurations are detailed in Sect. 3 and Sect. 4, respectively, and
113 the results are presented in Sect. 5. A discussion is proposed in Sect. 6. At the
114 end, a summary of findings is given and some future directions are discussed.

115 **2 Mesoscale Atmospheric Model Meso-NH for Obstacle-Resolving** 116 **Simulations**

117 2.1 The Meso-NH Model

118 The Meso-NH model (Lac et al. 2018) is a non-hydrostatic research atmo-
 119 spheric model, able to simulate atmospheric flows from the mesoscale (tens of
 120 kilometres and day-long phenomena) to the microscale (metres and second-
 121 long phenomena). The Meso-NH model is parallelized (Jabouille et al. 1999)
 122 and able to perform dynamical downscaling using the grid-nesting approach
 123 (Stein et al. 2000). The governing equations are based on the conservation
 124 laws for mass, momentum, energy, and on the ideal gas law. The Meso-NH
 125 model uses the anelastic approximation of the pseudo-incompressible system
 126 of Durran (1989), filtering the elastic effects from acoustic waves.

127 The domain is spatially discretized using the C-grid of Arakawa (Mesinger
 128 and Arakawa 1976). A conformal projection system and a regular grid size
 129 ($\Delta_x = \Delta_y = \Delta$) are used for the horizontal directions. The vertical grid is
 130 based on the terrain-following coordinates of Gal-Chen and Somerville (1975)
 131 which fit non-plane surfaces.

132 In the present study, a LES framework is used to estimate the Reynolds
 133 Stress term in the momentum equation. The LES closure is performed by
 134 the 1.5-order closure scheme described in Cuxart et al. (2000). This closure
 135 is based on the calculation of the subgrid turbulence kinetic energy ($e_{sb} =$
 136 $1/2(\overline{u'^2} + \overline{v'^2} + \overline{w'^2})$, where u' , v' , and w' are the x -, y -, and z -turbulence velocity
 137 components) through a prognostic equation and on a diagnostic adaptative
 138 mixing length (Honnert et al. 2021).

139 For the wind advection, Meso-NH uses either CEN4TH, a fourth-order
 140 centred scheme, or WENO5, a fifth-order weighted essentially non-oscillatory
 141 scheme. Explicit Runge–Kutta schemes are used for time integration (Lunet
 142 et al. 2017). The CEN4TH advection scheme should be used with a fourth-
 143 order Runge–Kutta (RKC4) time marching whereas WENO5 can be used
 144 together with a five-stage third-order Runge–Kutta (RK53) scheme. Explicit
 145 numerical diffusion is not appropriate with WENO5, whereas CEN4TH re-
 146 quires numerical diffusion, which is characterized by the e-folding time t_c of
 147 $2\Delta_x$ waves.

148 The advection of a prognostic scalar such as the pollutant is made by a
 149 piecewise parabolic method (PPM) based on the original Colella and Wood-
 150 ward (1984) scheme with monotonicity constraints modified by Lin and Rood
 151 (1996). The temporal algorithm of PPM is forward-in-time. Explicit numerical
 152 diffusion is not used either with the PPM scheme.

153 2.2 The Immersed Boundary Method in Meso-NH

154 Since the numerical solvers in Meso-NH enforce conservation on structured
 155 grids, they cannot handle body-fitted grids with steep topological gradients.

156 This is a common issue for meteorological models. Explicitly modelling the
157 fluid–solid interaction in the urban roughness sublayer, which extends up to
158 2–5 times the characteristic building height (Roth 2000) is necessary to capture
159 the relevant processes for the urban climate. To this end, a version of Meso-NH
160 including the IBM to represent the buildings, MNH-IBM, has been developed
161 by Auguste et al. (2019). The MNH-IBM version is currently restricted to
162 cartesian grids and flat terrains.

163 Within the MNH-IBM framework, the numerical domain is divided be-
164 tween two distinct regions: a fluid region where the classical fluid conservation
165 laws are applied and a solid region having a volume similar to the embedded
166 obstacles. The interface between the two regions is defined by a continuous
167 level-set function (Sussman et al. 1994), ϕ . The absolute value of ϕ gives the
168 minimal distance between a grid point and the interface. The sign of ϕ allows
169 for distinguishing between the solid ($\phi > 0$) and the fluid ($\phi < 0$) region.
170 The level-set function is restricted to non-moving interfaces and is not time-
171 dependent, which is not an issue when it comes to modelling urban environ-
172 ments.

173 Among the various IBM methods, a review can be found in Iaccarino and
174 Verzicco (2003) and Kim and Choi (2019), the fine resolution required close to
175 the interface led Auguste et al. (2019) to adopt an IBM method based on the
176 discrete forcing approach for MNH-IBM. The boundary conditions are spec-
177 ified at the immersed interface. This is achieved by forcing the conservation
178 equations at the vicinity of the embedded solid surfaces via two Cartesian grid
179 methods, a ghost-cell technique (Tseng and Ferziger 2003) and the cut-cell
180 technique (Yang et al. 1997). The ghost-cell technique corrects the explicit-in-
181 time schemes such as the advection and the diffusion schemes. It also computes
182 the prognostic variables (velocity, temperature, and e_{sb}) in the immersed solid
183 volume to satisfy the required boundary conditions at the interface. As an
184 example, a local log law with the appropriate material roughness is imposed
185 for the tangential velocity. The cut-cell technique corrects the pressure solver
186 and ensures the incompressibility constraint by modifying the right-hand side
187 of the Poisson equation. Finally, an iterative procedure is applied on the mod-
188 ified Poisson equation to ensure the interface non-permeability (Auguste et al.
189 2019).

190 The MNH-IBM implementation has been validated by Auguste et al. (2019)
191 for the MUST idealized urban-like environment, without pollutant transport,
192 realistic incoming turbulence or grid-nesting. In this study, MNH-IBM repro-
193 duced with reasonable accuracy the observed mean flow and turbulent fluctua-
194 tions within the urban roughness sublayer. The MNH-IBM code has also been
195 used to reproduce the dispersion of the pollutants plume generated by the
196 AZF (AZotes Fertilisants) fertilizer production plant explosion in Toulouse
197 (France) in September 2001 (Auguste et al. 2020). The model presented a
198 realistic plume dispersion and simulated a limited population’s exposure to
199 pollution, which appeared to be in good agreement with the health studies
200 performed on the AZF explosion.

2.3 The Turbulence Recycling in Meso-NH

One of the main bottlenecks encountered when performing multiscale LES simulations on nested grids is generating proper turbulence in the ABL. Indeed, a development fetch is needed within each domain to allow for the cascade of eddies of different scales in the inertial subrange to adapt to the new resolution (Muñoz-Esparza et al. 2014). Realistic turbulent inflow conditions must be generated to reduce this fetch. This has been an extensive research field over the last thirty years and numerous methods have been proposed. Among them, two are widely used: the cell perturbation method (Muñoz-Esparza et al. 2014, 2015), and recycling methods adapted from the original proposition of Lund et al. (1998). In the present study, the recycling method has been chosen for the sake of simplicity in the implementation.

The idea behind the recycling method of Lund et al. (1998) is simple. The prognostic variable fluctuations from a vertical plane parallel to the inflow boundary are calculated, extracted, and added to the variable field at the inlet. In several LES models, such as the Parallelized Large-Eddy Simulation Model (PALM, Maronga et al. 2015), the recycling method uses the modifications to the original proposition of Lund et al. (1998) introduced by Kataoka and Mizuno (2002): the fluctuations are calculated with respect to a constant altitude line average in the recycling plane. This method has been successfully used to study configurations with urban topography (Park et al. 2015a,b). However, as mentioned by Muñoz-Esparza et al. (2015), this method may present issues when the flow direction changes and is not easily generalized for multiple inflow boundaries. Moreover, performing a spatial average to calculate the fluctuations is not adapted to inhomogeneous main flow and turbulence.

In the present study, an alternative recycling method is introduced: the prognostic variable fluctuations from a vertical plane parallel to the inflow boundary are calculated with respect to a moving temporal average and these fluctuations are added to the prognostic variable field at the inlet. First, it must be ensured that the turbulence is resolved down to $M\Delta$ in the father model, M being ideally equal to 4 or 6, depending on the effective resolution of the father model (Skamarock 2004). The effective resolution of a model is the minimum wavelength correctly simulated by the model. In the nested son domain, the time window for the calculation of the moving temporal average (T_{recycl}) has to be sufficiently large for the fluid to be advected over a distance corresponding to about $M\Delta$ in the father model. Furthermore, to save computational time and memory, the variable average is calculated with a limited number of son domain timesteps (N) over T_{recycl} . The value of N should be sufficiently high to reduce the statistical uncertainty of the calculated moving average and sufficiently low in terms of memory requirements, since the N values for each grid point in the recycling plane need to be kept in memory.

Figure 1 shows a domain where inflow boundary conditions may be imposed at each lateral side (north, east, south, west). For the sake of clarity, we consider in the following that the flow is incoming from the west boundary, i.e.,

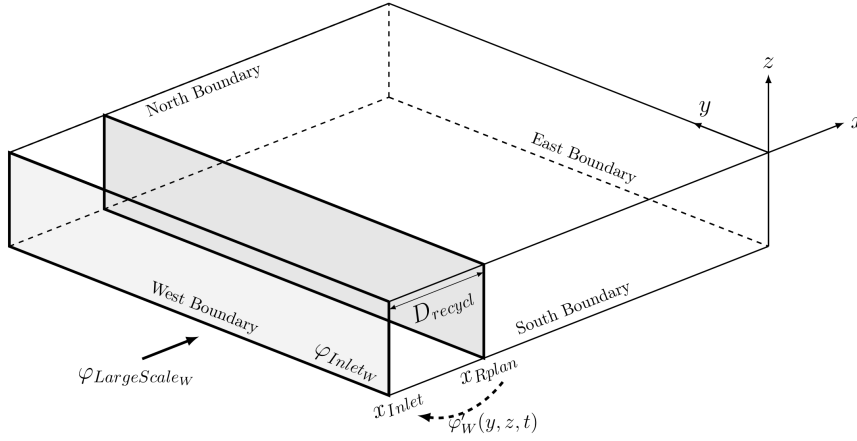


Fig. 1 Sketch of the turbulence recycling method used to generate turbulent inflow. For clarity, only the recycling of fluctuations at the west boundary is shown, but the same method applies on the four lateral sides

246 the recycling method is only applied on the west boundary. If needed, the same
 247 method could apply on the four lateral sides. A wind vector that is not aligned
 248 with the grid axis will thus be recycled on two sides. Considering the prognos-
 249 tic variable at the west boundary (W) $\varphi_W \in [u, v, w]$, the fluctuations φ'_W are
 250 calculated in the recycling plane being located at a distance D_{recycl} from the
 251 inlet. In the present work, since we are working on near-neutral cases, only the
 252 three velocity components are recycled. For other configurations, prognostic
 253 variables such as the temperature can be recycled. The fluctuations calculation
 254 reads:

$$\varphi'_W(y, z, t) = \varphi_W(x_{Rplan}, y, z, t) - \overline{\varphi_W(x_{Rplan}, y, z)}, \quad (1)$$

255 where $\varphi_W(x_{Rplan}, y, z, t)$ and $\overline{\varphi_W(x_{Rplan}, y, z)}$ are the instantaneous and the
 256 time averaged prognostic variable in one point of the recycling plane, respec-
 257 tively.

258 The value of $\varphi'_W(y, z, t)$ is added to the corresponding inflow prognostic vari-
 259 able, φ_{Inlet_W} :

$$\varphi_{Inlet_W}(y, z, t) = \varphi_{LargeScale_W}(y, z, t) + \varphi'_W(y, z, t)\beta\psi_W(y, z, t), \quad (2)$$

260 where $\varphi_{LargeScale_W}$ is the variable field imposed at the boundary, $\beta \in [0.1-$
 261 $0.25]$ a weighting coefficient preventing calculation divergence, and $\psi_W(y, z, t)$
 262 an inflow damping function:

$$\psi_W \rightarrow \begin{cases} 1 & ; \text{if } T_{BV} > T_{BV_{max}} \\ \frac{(T_{BV} - T_{BV_{min}})}{(T_{BV_{max}} - T_{BV_{min}})} & ; \text{if } T_{BV_{min}} \leq T_{BV} \leq T_{BV_{max}} \\ 0 & ; \text{if } T_{BV} < T_{BV_{min}} \end{cases}, \quad (3)$$

263 where T_{BV} is the calculated Brunt–Väisälä period, and $T_{BV_{max}}$ and $T_{BV_{min}}$
 264 are maximal and minimal allowed values of the Brunt–Väisälä period. Here,
 265 $T_{BV_{min}} = 2T_{BV_{nn}}$ and $T_{BV_{max}} = 3T_{BV_{nn}}$, where $T_{BV_{nn}} \approx 90$ s is the estimated
 266 Brunt–Väisälä period for the U.S. Standard Atmosphere.

267 The ψ_W function is calculated at the inlet; it is equal to 1 in neutral or
 268 near-neutral layers (e.g., in the boundary layer) and is linearly damped to 0
 269 in stable layers. Its purpose is twofold: filtering the fluctuations due to gravity
 270 waves and preventing the imposed fluctuations to be affected by a potential
 271 increase in boundary-layer height between the recycling plane and the inlet.
 272 The proposed recycling method has been successfully validated in Sect. 5.1 for
 273 a neutral ABL.

274 3 The Mock Urban Setting Test Experiment

275 3.1 Description

276 The Mock Urban Setting Test (MUST) experiment (Biltoft 2001; Yee and
 277 Biltoft 2004) is a near full-scale measurement campaign conducted during the
 278 month of September 2001 in Utah’s West desert, at the U.S. Army Dugway
 279 Proving Ground (40° 12.606’ N, 113° 10.635’ W). The site is located 1310 m
 280 above the mean sea level and can be considered flat. The MNH-IBM model,
 281 limited to Cartesian grids, can therefore be used to reproduce this experiment.

282 The MUST experimental campaign objective was twofold: study the dis-
 283 persion of a passive tracer through a large array of building-like obstacles and
 284 provide reference data for the validation of numerical models for dispersion of
 285 pollutants in urban areas.

286 Figure 2 shows a sketch of the experimental configuration. The MUST
 287 idealized urban-like environment consists of a near-regular array of 10×12
 288 ship-containers. Their dimensions are 2.42 m in width (L_x), 12.9 m in length
 289 (L_y), and 2.54 m in height (H) except for the one identified as H5, which is
 290 2.44 m wide, 6.1 m long, and 3.51 m high. The horizontal averaged distance
 291 between the containers is 12.9 m in the x -direction and 7.9 m in the y -direction.
 292 The array axis forms an angle of 30° to the north. The desert vegetation
 293 surrounding the containers has an aerodynamic roughness length $z_0 = 0.045$
 294 m (Yee and Biltoft 2004).

295 The MUST experimental procedure consists of 900-s-long releases of propy-
 296 lene (C_3H_6). This procedure has been repeated for different incoming wind
 297 directions and pollutant release locations; 21 cases are presented in Yee and
 298 Biltoft (2004). The locations of the different instruments used for compari-
 299 son with model results in the present study are given in Fig. 2. The veloc-
 300 ity and turbulence measurements have been performed using two- and three-
 301 dimensional sonic anemometers. They were placed at different heights upwind
 302 (mast S), downwind (mast N), within and above the container array. Concern-
 303 ing the pollutant, 72 detectors have been used to measure its concentration
 304 within and above the array. Horizontally, 40 photo-ionization detectors (PIDs)

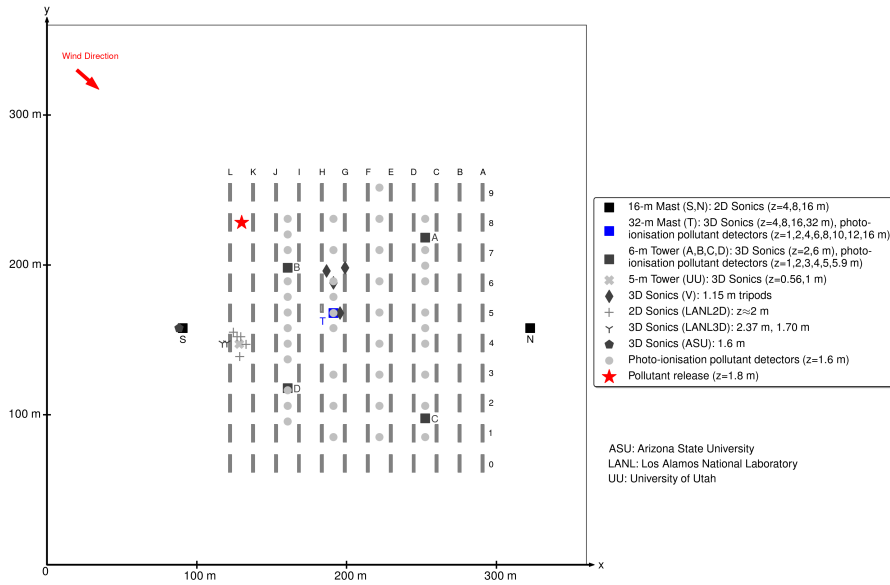


Fig. 2 Sketch of the MUST experiment including the location of the different instruments. The figure is adapted from Yee and Biltoft (2004) and Milliez and Carissimo (2007)

305 were located on four lines (light grey dots in Fig. 2) at height $z = 1.6$ m. Eight
 306 PIDs were mounted on the 32-m tower (T) and six ultraviolet ion collectors
 307 (UVICs) were mounted on each of the four 6-m towers (A, B, C, D) to obtain
 308 vertical pollutant concentration profiles.

309 3.2 Selected Case

310 We reproduce the MUST case number 2681829, starting 25 September 2001
 311 at 1830 LT (local time = UTC-6 h). It was chosen because the atmosphere
 312 is in a near-neutral state, the Obukhov length (L_{MO}) being 28,000 m.

313 In order to prevent the results from being influenced by the unsteadiness
 314 of the atmospheric conditions, previous CFD simulations of the MUST case
 315 (Milliez and Carissimo 2007; Dejoan et al. 2010) were compared with the
 316 200 s quasi-steady periods extracted by Yee and Biltoft (2004) within each
 317 900-s plume dispersion experiment. As the focus of the present study is to
 318 investigate the influence of the ABL turbulence on the wind conditions and
 319 pollutant transport in the container array, the complete 900-s time period of
 320 pollutant release is investigated.

321 Table 1 gives information on the chemical substance release, the mean flow
 322 and the turbulence characteristics. The mean incident wind direction angle
 323 is equal to -40° with respect to the x -direction (Fig. 2). The tracer gas is
 324 released in the upstream part of the container array (Fig. 2, red star symbol)
 325 at a height of 1.8 m and at a constant flowrate of 225 L min^{-1} .

Table 1 Information on chemical substance release, main flow, and turbulence characteristics. The official case name is its date in the Julian calendar, 2681829 (25/09/2001). It is also named “trial 11” in Yee and Bilitoft (2004). Here, $\overline{U_{04}}$ is the time-averaged wind speed, $\overline{\alpha_{04}}$ is the time-averaged wind mean direction at 4 m height on the upwind mast S, Q is the tracer release rate at the source, and x_s, y_s, z_s is the location of the source with respect to the coordinate system defined in Fig. 2

Start Time (LT)	$\overline{U_{04}}$ (m s ⁻¹)	$\overline{\alpha_{04}}$ (°)	L_{MO} (m)	(x_s, y_s, z_s) (m, m, m)	Q (L min ⁻¹)
1830	7.9	-40	28,000	(129.87, 228.35, 1.8)	225

326 4 Numerical Configurations

327 Three numerical configurations are studied. The MNH-IBM code is first used
 328 as in a typical CFD configuration, i.e., without accounting for the large-scale
 329 ABL turbulence. The first CFD-like configuration has a limited vertical ex-
 330 tension of 40 m, whereas the second configuration simulates the entire ABL
 331 and extends up to 3000 m above ground level (a.g.l.) (i.e., 4310 m above mean
 332 sea level). In the third configuration, the large-scale atmospheric turbulence
 333 prevailing in the ABL is accounted for, thanks to nested domains with increas-
 334 ing horizontal resolution. In all configurations, the pollutant is considered as
 335 a passive scalar and its density difference with air is not accounted for, since
 336 the maximum pollutant concentrations are very small.

337 4.1 Computational Fluid Dynamics-like Configurations

338 The first CFD-like configuration (called CFD40) intends to reproduce what
 339 is typically done in obstacle-resolving scale CFD simulations. Two important
 340 simplifications are performed. First, the observed wind profile is imposed at
 341 the boundary. Second, the top of the domain is fixed at $z \approx 40$ m, which
 342 corresponds approximatively to sixteen times the obstacles height. A domain
 343 top much lower than the ABL height is common in urban CFD simulations;
 344 the best practice guideline given by Franke et al. (2011) recommends using at
 345 least a domain six times higher than the tallest building.

346 Figure 3 schematically represents the CFD40 configuration: the containers
 347 are within a 360 m side square domain. The mesh is cartesian, with a horizontal
 348 resolution $\Delta_x = \Delta_y = 0.3$ m. In the vertical direction, for $z < 6$ m the
 349 vertical grid size is constant and $\Delta_z = 0.3$ m. Above 6 m, it increases with a
 350 constant geometric ratio of 1.095. The blockage ratio of the obstacles and the
 351 distance from the boundaries of the computational domain to the container
 352 array respect the Franke et al. (2011) guideline.

353 A steady velocity profile is imposed at the domain boundaries. It is con-
 354 structed by fitting a log-law to the S tower observations, which are upstream
 355 of the container array. The incoming flow has a mean horizontal angle of -40°
 356 with respect to the x -direction, it only enters in the domain by the west and
 357 north boundaries.

358 The containers are represented with the IBM. The ground friction of the
 359 surrounding vegetation, characterized by an aerodynamic roughness length
 360 $z_0 = 0.045$ m, is modelled with the externalized surface scheme SURFEX
 361 (Masson et al. 2013). The turbulent fluxes of sensible and latent heat at the
 362 surface are prescribed as 0.0 W m^{-2} .

363 The turbulence recycling method is used at the west and north boundaries
 364 in order to generate a turbulent incoming flow. Here, $\beta = 0.25$ and since
 365 there is no father domain, a very low value of $T_{recycl} = 56$ corresponding
 366 to 1.12 s is chosen. The recycling plane is placed 30 m from the boundaries.
 367 As shown in Fig. 3, the velocity turbulent fluctuations are calculated in the
 368 vertical planes x_{Rplan_W} and y_{Rplan_N} and added to the inflow velocity field at
 369 the west and north boundaries, respectively. In this CFD-like configuration,
 370 the incoming flow contains small-scale turbulent structures only. It is therefore
 371 not representative of the ABL turbulence.

372 The WENO5 and RK53 schemes are used for the wind advection and
 373 the time marching. The WENO5 scheme has been selected because it is well
 374 adapted to sharp gradient areas (Lunet et al. 2017). Furthermore, the CFD40
 375 configuration has no absorbing layer in the upper part of the domain as this
 376 case is purely neutral.

377 The second CFD-like configuration, named hereafter CFD3000, presents
 378 two differences compared to CFD40. First, the domain extends vertically to
 379 3000 m a.g.l. Similarly to CFD40, for $z < 6$ m, the vertical grid size is constant
 380 with $\Delta_z = 0.3$ m. Above 6 m, the vertical grid size increases with a constant
 381 geometric ratio of 1.095 until Δ_z reaches 50 m. The case is near neutral up
 382 to 1500 m a.g.l. where an inversion layer is imposed. A Rayleigh relaxation
 383 layer is located above $z = 2000$ m to damp gravity waves. Secondly, since a
 384 logarithmic profile up to 3000 m a.g.l. is not a sustainable hypothesis, the
 385 CFD3000 case is forced with a velocity profile extracted from the multiscale
 386 configuration (Sect. 4.2).

387 For the two cases, the ceiling of the domain is rigid, corresponding to a free-
 388 slip condition. A summary of both CFD-like numerical configurations' main
 389 parameters is given in Table 2.

390 4.2 Multiscale Configuration

391 For the multiscale configuration (MSC), the mesoscale turbulence prevailing
 392 in the ABL is accounted for by using four nested domains with increasing hor-
 393 izontal resolution (Fig. 4). A one-way grid-nesting approach is used: the father
 394 domain variables influence the son domain variables but not vice-versa. The
 395 coarsest domain, D1, is a 76.8 km side square. It has a horizontal resolution
 396 of 96 m. Cyclic boundary conditions are employed for D1, therefore, from a
 397 physical point of view, its horizontal extent is infinite. Due to its coarse reso-
 398 lution, only the largest eddies of the neutral ABL are resolved in D1. The flow
 399 results from a balance between the Coriolis force, a geostrophic wind which
 400 represent the large scale pressure gradient and the surface friction. The grid-

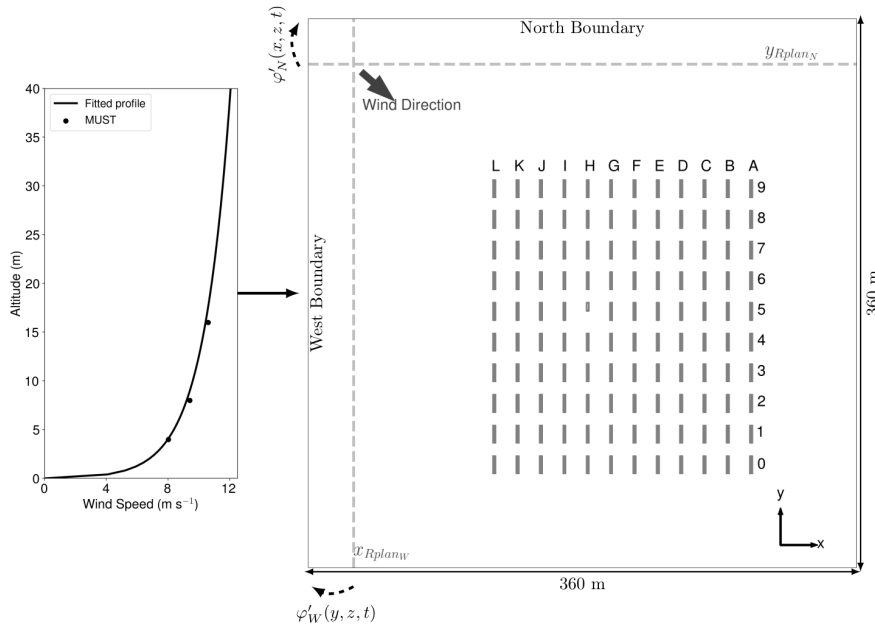


Fig. 3 Domain extent and inflow wind profile for the CFD40 configuration. A logarithmic velocity profile based on the experimental measurements profile is prescribed at the west and north boundaries. The turbulence recycling method is applied at these boundaries

401 nesting method is used for the lateral boundaries of the three finer domains.
 402 The domains 2 (D2) and 3 (D3) are 19.2 km and 2.4 km side squares with a
 403 horizontal resolution of 24 m and 3 m, respectively. Finally, the finest domain,
 404 D4, has the horizontal dimensions and resolution of the CFD-like configura-
 405 tions domain (Sect. 4.1). The vertical extent of all the nested domains is 3000
 406 m a.g.l. in order to simulate the entire ABL for this desert site in early autumn.
 407 The vertical grid and top boundary conditions are identical to the CFD3000
 408 ones. The predominant wind direction being known, D3 and D4 are placed in
 409 the bottom right part (with respect to the cartesian system represented in Fig.
 410 4) of their parent domain. This is a common method to reduce the transition
 411 fetch between two nested domains (e.g., Wiersema et al. 2020).

412 In all the domains, the ground friction is characterized by an aerodynamic
 413 roughness length $z_0 = 0.045$ m and modelled with the SURFEX scheme (Mas-
 414 son et al. 2013). Except for the domain top height, the vertical grid and the
 415 boundary conditions, D4 has the same characteristics as the single domain
 416 employed for the CFD-like configurations.

417 The turbulence recycling method is used to enhance the turbulence scale
 418 transition between two nested subdomains. In D2 and D3, as shown in Fig.
 419 4, the velocity fluctuations are added to the large-scale velocity fields coming
 420 from the father domain at the west and north boundaries. It has been found

421 that between D3 and D4, the turbulence scale transition naturally happens
 422 within a very reduced fetch. The turbulence recycling is therefore not used in
 423 D4.

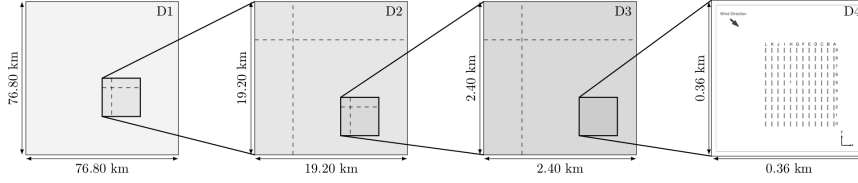


Fig. 4 Illustration of the MSC approach. The recycling method is applied on the west and north boundaries of domains D2 and D3. The dashed lines indicate the positions of the recycling vertical planes

424 Numerically, CEN4TH/RKC4 is used for D1, D2, and D3 because is it the
 425 more appropriate combination to perform LES of the ABL (Lac et al. 2018).
 426 Similar to the CFD-like configurations, WENO5/RK53 is used for D4. In all
 427 domains, an inversion layer is imposed at $z = 1500$ m and a Rayleigh relaxation
 428 layer is located above $z = 2000$ m. A summary of the numerical configurations
 429 is given for each domain in Table 2.

Table 2 Numerical configurations main parameters. GW: geostrophic wind. FD: wind coming from the father domain. IWP: Idealized wind profile. EWP: wind profile extracted from MSC. t_c : e-folding time of the $2\Delta_x$ waves

Parameter	D1	D2	D3	D4	CFD40	CFD3000
Δ_x and Δ_y (m)	96	24	3	0.3	0.3	0.3
Timestep (s)	1.2	0.24	0.04	0.02	0.02	0.02
Time integration scheme	RKC4	RKC4	RKC4	RK53	RK53	RK53
Wind advection scheme	CEN4TH	CEN4TH	CEN4TH	WENO5	WENO5	WENO5
t_c (s)	1800	100	10	None	None	None
Boundary-conditions	Cyclic	Open	Open	Open	Open	Open
Wind boundary-conditions origin	GW	FD	FD	FD	IWP	EWP
Turbulence recycling	No	Yes	Yes	No	Yes	Yes

430 5 Results

431 5.1 Validation of the Turbulence Recycling Method

432 The turbulence recycling method described in Sect. 2.3 is here validated for
 433 the neutral conditions corresponding to the selected MUST case. For this
 434 purpose, a preliminary configuration is used, which is different from the MSC

435 as it includes only two nested domains. The domain 1 presented in Sect. 4.2
 436 is the father domain. The son domain has the resolution of D2, but its side
 437 length is reduced to 9600 m. The CEN4TH/RKC4 set-up is employed in both
 438 domains.

439 A 200000-s simulation is conducted for D1, a simulation duration sufficient
 440 for the establishment of the geostrophic wind balance and the development of
 441 the largest eddies of the neutral ABL. The effective resolution of D1, defined
 442 via the turbulence spectrum in the inertial subrange is 4Δ (not shown but
 443 in agreement with Lac et al. 2018 for to the 4th-order advection scheme). In
 444 the son domain, the velocity fluctuations are added to the large-scale velocity
 445 fields coming from the father domain at the west and north boundaries. The
 446 fluctuations are calculated in vertical planes placed at 2400 m (equivalent
 447 to one fourth of the domain size) of the boundary. The velocity fluctuation
 448 average is calculated over $N = 28$ timesteps, which corresponds to 672 s.

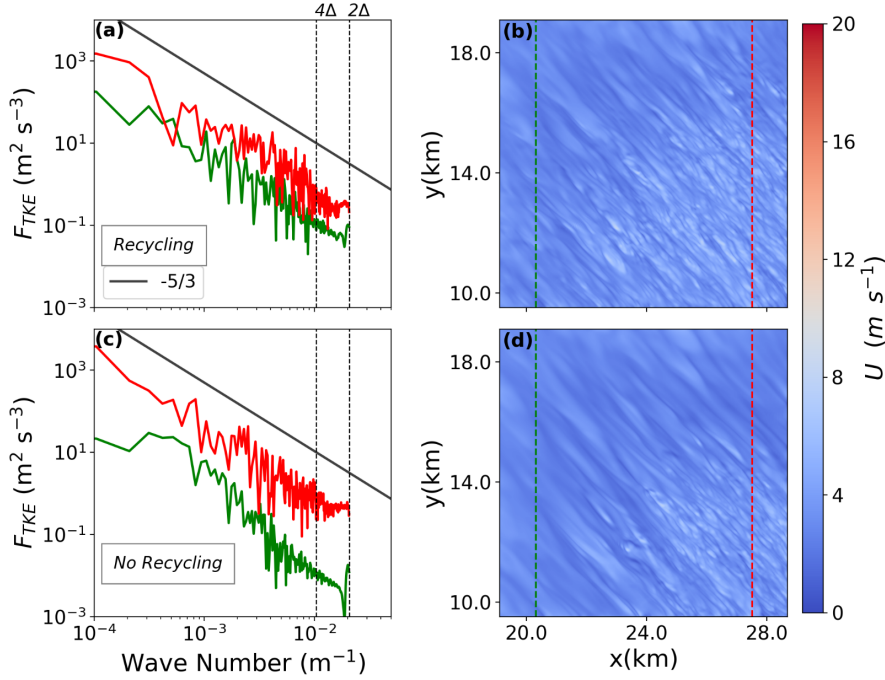


Fig. 5 The TKE spectrum at $z = 500$ m (a,c) and wind speed at $z = 1.5$ m (b,d) in the son domain after 30000 s of dynamics using the turbulence recycling method (a,b) or not (b,c). Green and red dashed lines in the right column show where the corresponding color TKE spectrum is calculated. The full black line in the spectrum plots is the Kolmogorov $-5/3$ slope

449 Figure 5 shows the effects of the turbulence recycling on the wind speed
450 at $z = 1.5$ m (Fig. 5b, d) and the turbulence kinetic energy (TKE) spectrum
451 at $z = 500$ m (Fig. 5a, c) in the son domain after 30000 s. For the wind
452 speed at $z = 1.5$ m, when using the turbulence recycling method, small-scale
453 turbulent structures are present in a large part of the domain, except close to
454 the inlet boundaries. Without the turbulence recycling method, these small-
455 scale turbulent structures are only present at the bottom right corner of the
456 domain. These turbulent structures close to the ground change the incoming
457 flow in the container array. The same transition improvement is found all along
458 the vertical direction.

459 Green and red dashed lines in Fig. 5b and d show where the correspond-
460 ing colour TKE spectrum is calculated. When using the turbulence recycling
461 method, the turbulence is at scale in the son domain. By “at scale” we mean
462 that the turbulence in the inertial subrange is well developed and that the
463 turbulence spectrum follows Kolmogorov’s $k^{-5/3}$ law until $4\Delta_x$. With the tur-
464 bulence recycling method, this is true even close to the west and north bound-
465 aries (see the green spectrum). This is not the case without the turbulence
466 recycling method, where the turbulence at scale is restricted to the areas close
467 to the east and south boundaries.

468 The turbulence recycling method thus allows the reduction of the fetch and
469 efficiently improves the turbulence scale transition when using nested grids.

470 5.2 Wind Speed, Wind Direction, and Turbulence Kinetic Energy in the 471 Surface Layer Upstream of the Container Array

472 Figure 6 shows the 900-s-average vertical profiles in the surface layer of the
473 wind speed (Fig. 6a), wind direction (Fig. 6b), and total TKE (Fig. 6c) at the
474 S tower located upstream of the container array (Fig. 2).

475 Concerning both CFD-like configurations, the wind speed profiles match
476 very well the observations from Yee and Biltoft (2004). The agreement is also
477 satisfactory for the wind direction. The TKE is underestimated all along the
478 vertical. It must however be recalled here that, contrary to RANS CFD models,
479 no TKE boundary conditions can be imposed in Meso-NH. In these configura-
480 tions, the TKE is mainly obtained thanks to the turbulence recycling method.
481 A simulated TKE that is in the same order of magnitude as the experimen-
482 tal results remains therefore acceptable. The profiles are very similar between
483 both CFD-like configurations, showing that the domain height has no impact
484 on the incoming wind profile.

485 Concerning the MSC, the wind speed and the wind direction profiles are
486 in very good agreement with the observations in the surface layer. The MSC’s
487 TKE profile agrees well with the observations. It shows that the turbulence is
488 well captured upstream of the container array.

489 Figure 7 shows the temporal evolution of the wind speed and direction at
490 tower S for the 900 s of the pollutant release, for $z = 4$ m and $z = 16$ m. The
491 temporal resolution is 0.1 s for the numerical simulations and the observations.

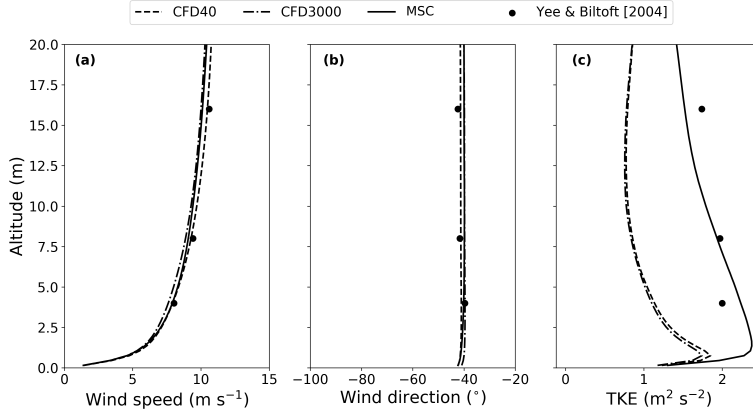


Fig. 6 Average (900 s) vertical profiles of wind speed (a), wind direction (b), and TKE (c) at the S tower location upstream of the container array (Fig. 2)

492 The observed wind direction variability is less important at $z = 16$ m than
 493 at $z = 4$ m. This is well captured by the two CFD-like and the MCSs. For
 494 the sake of clarity, only CFD40 is shown. The results are almost identical for
 495 CFD3000.

496 For a more quantitative comparison, the mean and standard deviation of
 497 the series are compared in Table 3. The time-averaged wind speed is in excel-
 498 lent agreement with the observations, especially for the CFD40 and the MSCs.
 499 At $z = 4$ m, CFD40 simulates an averaged wind direction slightly shifted about
 500 2° to the right (from a wind flow point of view). On the contrary, at $z = 16$ m,
 501 MSC and CFD3000 (which is forced by a velocity profile extracted from MSC)
 502 simulate an average wind direction shifted about 2° to the left. However, the
 503 overall agreement remains very satisfactory for both configurations.

504 Both CFD-like configurations underestimate the standard deviation for
 505 each quantity, at both altitudes, whereas the agreement is very good for the
 506 MSC. This can also be seen in Fig. 7, where fluctuations in wind speed and
 507 wind direction are more monotonous for CFD40 and CFD3000 than for MSC.
 508 This is particularly visible at $z = 16$ m where the low-frequency oscillations
 509 are reproduced with the MSC only. These low-frequency variations are char-
 510 acteristic of large ABL turbulent eddies of several minutes time scale crossing
 511 the probes.

512 Figure 8 shows the instantaneous wind speed at $z = 1.6$ m in the four nested
 513 domains of the MSC. The recycling method is effective since the transition
 514 fetch is limited to about one quarter of the model domain distance to the
 515 west and north boundaries in D2 and D3. For both of these domains, the
 516 transition fetch is halved when using the turbulence recycling method (not
 517 shown). Furthermore, ABL turbulence is simulated upstream of the container
 518 array in D4. This is not the case for the CFD-like configurations (not shown).

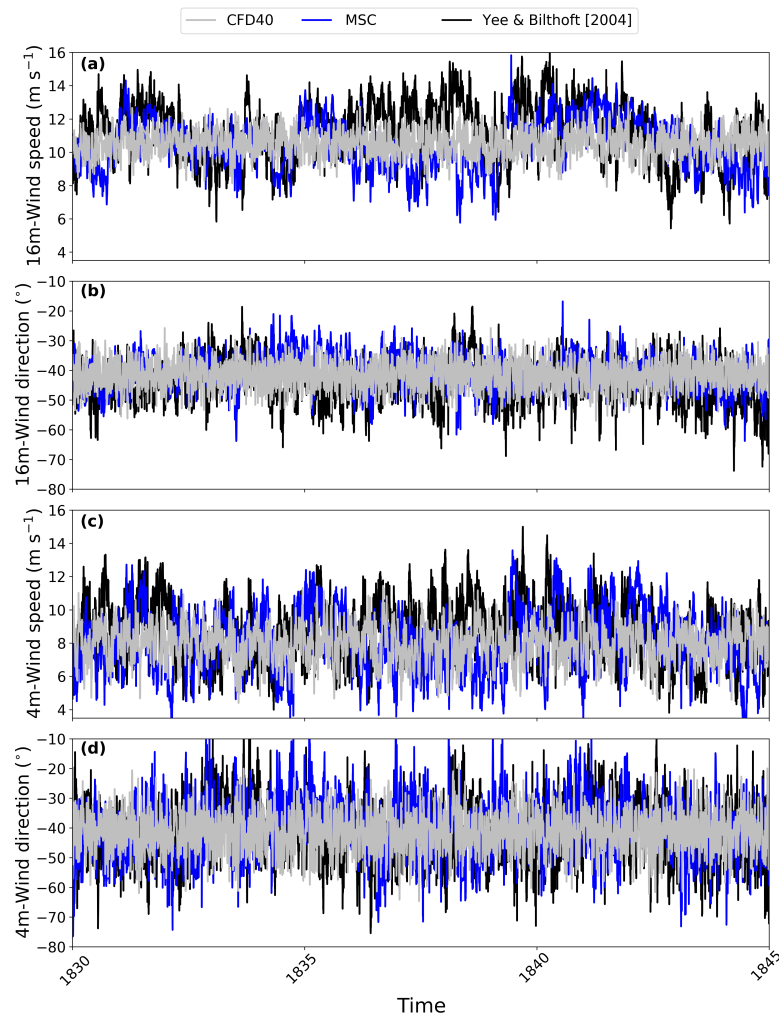


Fig. 7 Temporal evolution of the wind speed and wind direction at 16 m a.g.l. (a,b) and 4 m a.g.l. (c,d) for tower S located upstream of the container array. The temporal resolution is 0.1 s for the numerical simulations and the observations

519 The mean incoming wind conditions for the two CFD-like and multiscale
 520 configurations agree with the observations. The largest turbulent eddies oc-
 521 ccurring in the ABL are present in the MSC only. This allows investigation of
 522 the effects of the large ABL turbulent structures on the pollutant dispersion
 523 within the container array.

Table 3 Summary of the time average and standard deviation of the sample for the wind speed and direction at tower S located upstream of the container array. “Experiment” corresponds to the observations from Yee and Bilitoft (2004)

Case	$\overline{U_{04}}$ (m s ⁻¹)	$\sigma(U_{04})$ (m s ⁻¹)	$\overline{\alpha_{04}}$ (°)	$\sigma(\alpha_{04})$ (°)	$\overline{U_{16}}$ (m s ⁻¹)	$\sigma(U_{16})$ (m s ⁻¹)	$\overline{\alpha_{16}}$ (°)	$\sigma(\alpha_{16})$ (°)
Experiment	8.0	1.6	-39.7	8.6	10.6	1.5	-42.4	5.9
CFD40	8.0	1.1	-41.2	6.5	10.5	0.8	-41.5	4.5
CFD3000	7.7	1.1	-39.6	6.7	10.1	0.8	-40.0	4.5
MSC	8.1	1.9	-40.1	9.6	10.4	1.5	-40.5	5.8

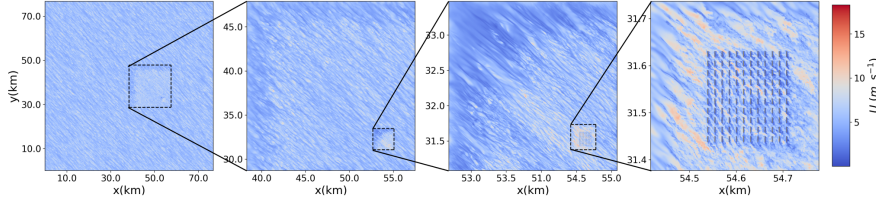


Fig. 8 Instantaneous ($t = 780$ s) wind speed at $z = 1.6$ m in the four nested domains of the MSC

5.3 Wind Speed, Wind Direction, and Turbulence Kinetic Energy Within and Above the Container Array

Figure 9 shows the 900-s-average vertical profiles of wind speed (Fig. 9a), wind direction (Fig. 9b), and TKE (Fig. 9c) at the mast T located within the container array (Fig. 2). The MSC agrees well with the observations all along the vertical. It is able to reproduce with high accuracy the wind speed reduction below $z = 10$ m due to the presence of the containers. Although less accurate, the CFD-like configurations also perform well below $z = 10$ m, but CFD40 overestimates the wind speed above $z = 10$ m whereas CFD3000 slightly underestimates it. Concerning CFD40, the overestimation is more pronounced at $z = 32$ m and is due to the unrealistic presence of a model top at $z = 40$ m.

The wind direction below $z = 3$ m, i.e., inside the container array, is similar for all configurations. Its values deviate from the upstream values of -40° to reach -100° , indicating that, at mast T, the wind within the container array is almost aligned with the y -direction. This is due to the fact that mast T is located in the recirculation cell of a container. Directly above the container height the wind direction corresponds to the inlet wind direction ($\approx -40^\circ$) for all configurations. This turning effect below the canopy height has been previously noticed by Yee and Bilitoft (2004) and Milliez and Carissimo (2007).

All configurations present slight discrepancies in the vertical TKE profiles. The MSC and CFD40 configurations underestimate the TKE above $z = 10$ m and $z = 4$ m, respectively. In the container array, below $z = 4$ m, both configurations display similar TKE profiles but overall, the MSC agrees better with

547 the observations. The CFD3000 TKE profile matches the CFD40 one between
 548 4 and 25 m. Above $z = 25$ m, CFD40 deviates because of the roof presence.
 549 Below $z = 4$ m, CFD3000 underestimates the TKE in a more pronounced way
 550 than CFD40.

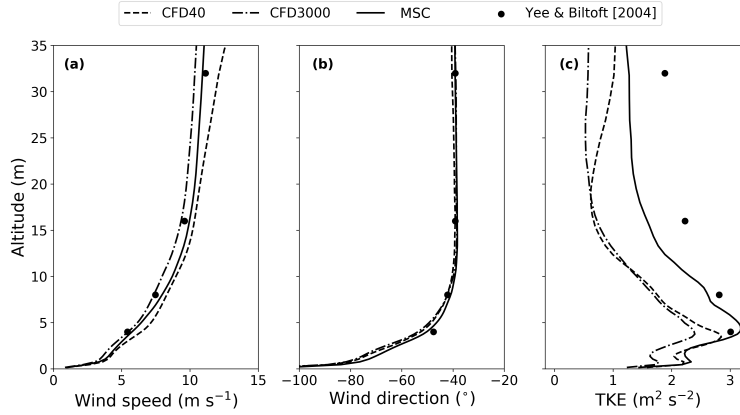


Fig. 9 Average (900 s) vertical profile of wind speed (a), wind direction (b), and TKE (c) at mast T located inside the container array (Fig. 2)

551 The overall good agreement between the presented numerical results and
 552 the literature shows that MNH-IBM and particularly the MSC are able to
 553 accurately simulate the average and standard deviation of wind speed and
 554 direction, and the TKE within and above the MUST container array.

555 5.4 Pollutant Dispersion

556 Figure 10 shows the pollutant concentration averaged over 900 s at $z = 1.6$
 557 m for the CFD40 (Fig. 10a, c) and the MSC approaches (Fig. 10b, d). The
 558 coloured circles indicate the observed values at the 40 PIDs probes located at
 559 $z = 1.6$ m. The full lines represent the 0.1 parts per million (ppm) iso-line
 560 of pollutant concentration. The wind speed is represented with a quiver plot
 561 in Figs 10c and d. The CFD3000 results (not shown on Fig. 10) are almost
 562 identical to the CFD40 ones.

563 The spread of the plume differs between the configurations. The CFD-like
 564 configurations are less dispersive than the multiscale one and underestimate
 565 the lateral plume spreading. The container array is also only slightly modifying
 566 the flow direction. This phenomenon has already been observed by Rochoux
 567 et al. (2021) with the MNH-IBM model. It has important consequences for
 568 the pollutant plume deflection. Indeed, as shown in the observations and in
 569 several numerical results (Milliez and Carissimo 2007; Dejoan et al. 2010),
 570 the containers induce a deflection of the mean pollutant plume axis relative

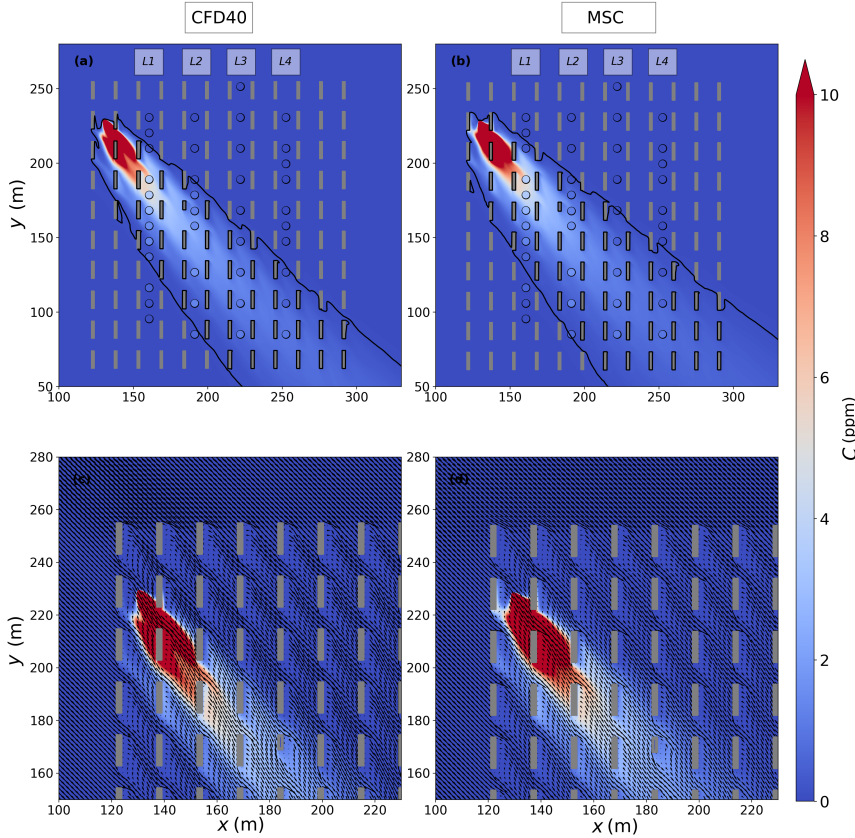


Fig. 10 Pollutant concentration averaged over 900 s at $z = 1.6$ m for the CFD40 (a and c) and the multiscale (b and d) configurations. The coloured circles indicate the observed values at the 40 PIDs probes. The full lines show the 0.1 ppm iso-line of pollutant concentration. The velocity vectors averaged over 900 s at $z = 1.6$ m for the CFD40 (c) and the multiscale (d) configurations are also displayed for a subdomain close to the inflow boundary in the lower line

571 to the inflow wind direction. For the MUST case 2681829, this deflection is
 572 particularly pronounced between container rows L to I (Fig. 8. of Milliez and
 573 Carissimo 2007), where the pollutant is channelled with the flow perpendicular
 574 to the x -axis of the container array. A comparison between our Fig. 10
 575 and the Fig. 8. of Milliez and Carissimo (2007) shows that MNH-IBM underestimates
 576 the plume deflection close to the pollutant source location for
 577 all configurations. The reason can be found in the flow pattern. The velocity
 578 quivers show the presence of recirculation cells downstream of the containers
 579 but also of strong jets rushing between the containers. The pollutant plume
 580 is subject to a competition between the recirculation cells that drive it per-
 581 pendicular to the x -axis (this happens at mast T for instance) and the jets
 582 that are almost aligned with the upstream wind. The jets, because of their

583 higher velocity, separate the different recirculation cells, the y -axis momen-
584 tum induced by the recirculation is broken and the pollutant is advected to
585 the next container street. The jets are therefore reducing the y -axis deflection
586 of the plume and its spreading on the horizontal directions. With MNH-IBM,
587 the jets are probably too strong and they cause an underestimation of the
588 pollutant plume deflection. We do not have a clear explanation of what causes
589 this phenomenon but it is possible that the lift effect that should be generated
590 by the elongated face of each container is underestimated. More investigations
591 should be carried on to properly explain this flaw. However, this is beyond the
592 scope of the present paper.

593 Figure 11 shows the 900-s-average concentration at $z = 1.6$ m along the
594 lines 1 (Fig. 11a), 2 (Fig. 11b), 3 (Fig. 11c), and 4 (Fig. 11d). The two CFD-
595 like configurations present very similar results and are analyzed together. For
596 probe lines 1, 2, and 3, the CFD-like configurations overestimate the maximum
597 value of pollutant concentration, which is located at the plume centreline. This
598 overestimation is more important for lines 1 and 2, i.e., close to the source
599 location. The left edge of the plume (from a wind flow point of view, i.e., right
600 of the figure) position is always well located. However, because the model is not
601 dispersive enough, the horizontal expansion of the plume is underestimated.
602 This has few consequences for line 1 where the right edge position of the plume
603 is well captured. But, when moving away from the release point (lines 2, 3,
604 and 4), the right edge position of the plume is shifted in space and pollutant
605 concentrations are underestimated at these locations. As a consequence, the
606 position of the maximum pollutant concentration is also shifted to the left
607 (from a wind flow point of view) for lines 2, 3, and 4. These observations are
608 consistent with those shown in Fig. 10 and highlight the main issue of the
609 CFD-like configurations, which are not sufficiently dispersive.

610 The MSC results are in slightly better agreement with the observations. For
611 lines 1 and 2, the edge of the plume is still well located and the maximum value
612 of pollutant concentration is less overestimated (especially for line 2) than for
613 the CFD-like configurations. It is in good agreement with the observations for
614 line 3 but underestimated for line 4. As for the CFD-like configurations, the
615 left edge of the plume is always well located, but when moving away from the
616 source, the concentration in the right side of the plume is underestimated and
617 the position of the maximum concentration is shifted in space. The dispersion
618 of the pollutant is however slightly better simulated than for the CFD-like
619 configurations. This is particularly true for lines 1 and 2, where MSC presents
620 fewer errors than the CFD-like configurations at the right edge of the plume
621 (left of the figure). This is consistent with the plume presented in Fig. 10.

622 Figure 12 shows the 900-s-average vertical profiles of pollutant concentra-
623 tion along mast T (Fig. 12a), towers B (Fig. 12b), and D (Fig. 12c). Tower
624 A is not taken into account because it is outside the dispersion plume extent
625 (see Fig. 2). Similar to Fig. 11, the two CFD-like configurations present very
626 similar results and are analyzed together.

627 For the CFD-like configurations, the pollutant concentration is overesti-
628 mated below $z = 12$ m at the mast T location, all along the vertical for tower

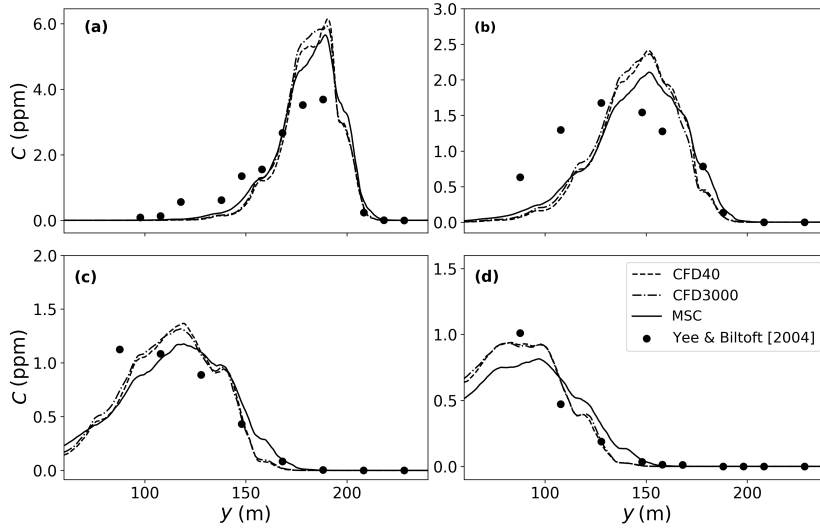


Fig. 11 900-s average pollutant concentration (C) at $z = 1.6$ m along the lines 1 (a), 2 (b), 3 (c), and 4 (d)

629 B, whereas it is underestimated for all probes at tower D. The agreement of
 630 the vertical profiles of pollutant concentration between the CFD-like configura-
 631 tion and the observations is poor but this can be expected in regards of the
 632 deficiencies in the horizontal plume spreading. Indeed, for the two CFD-like
 633 configurations, the mast T is located close to the plume centreline, where,
 634 because the configuration is not dispersive enough, these configurations over-
 635 estimate the pollutant concentration. This lack of dispersion can also explain
 636 the concentration underestimation at tower D, located at the right edge of the
 637 pollutant plume.

638 For the MSC, the results are in better agreement with the observations at
 639 mast T, even if the pollutant concentration is also overestimated below $z = 10$
 640 m. At tower B, the concentration is overestimated by a factor of 2 for all probes.
 641 For tower D, the multiscale results are improved compared with the CFD-like
 642 ones. However, the concentration is still underestimated compared with the
 643 observations. This is, once again, probably caused by the underestimation of
 644 the horizontal dispersion.

645 Overall, in terms of pollutant concentration, CFD-like and multiscale re-
 646 sults differ only slightly and are both in good agreement with the observations.
 647 The MSC results agree slightly better with the observations than the CFD-like
 648 ones for both horizontal and vertical probes. Taking into account the large-
 649 scale turbulent structures of the ABL seems therefore to also improve the
 650 concentration results, but only slightly. Moreover, the results for towers B and
 651 D are still unsatisfactory with the MSC. These points are further discussed in
 652 Sect. 6.

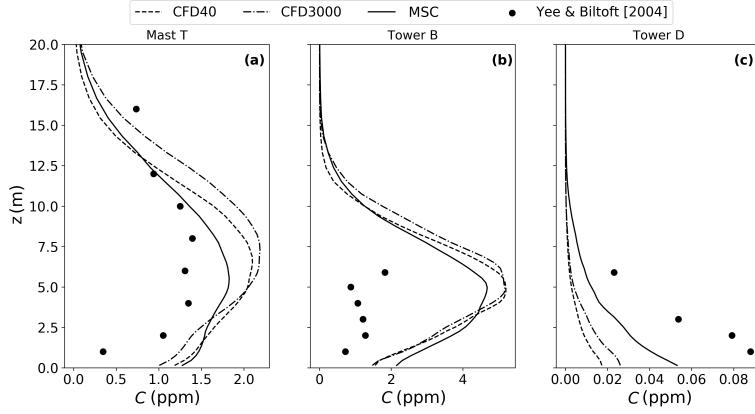


Fig. 12 Vertical profiles of 900-s-average pollutant concentration along mast T (a) and towers B (b), and D (c)

653 6 Discussion

654 The results presented in Sect. 5 show that MNH-IBM is able to qualitatively
 655 capture the observed pollutant concentrations for the selected MUST exper-
 656 iment. From a qualitative point of view, the MSC results are in better agree-
 657 ment with the observations than the CFD-like ones. In this section, the results
 658 are analyzed from a quantitative point of view and thoroughly discussed.

659 6.1 Skill Scores

660 The model performance for the average wind speed is evaluated with the hit
 661 rate (HR), adapted from Cox et al. (1998), it is expressed as the fraction of
 662 data where the averaged simulated wind speed is within a ± 1 m s $^{-1}$ range
 663 from the observation:

$$HR = \frac{1}{N_t} \sum_{i=1}^{N_t} N_i \text{ with } N_i = \begin{cases} 1 & \text{if } |\overline{U_{p_i}} - \overline{U_{o_i}}| \leq 1 \text{ m s}^{-1} \\ 0 & \text{else} \end{cases}, \quad (4)$$

664 where N_t is the number of samples, and $\overline{U_p}$ and $\overline{U_o}$ are the simulated and
 665 observed time-averaged wind speed, respectively. A perfect model would result
 666 in $HR = 1$.

667 The model performance for the wind direction is evaluated with the scaled
 668 average angle difference (SAA) originally proposed by Calhoun et al. (2004):

$$SAA = \frac{\sum (\overline{U_{p_i}} | \overline{\alpha_{p_i}} - \overline{\alpha_{o_i}} |)}{N_t \langle \overline{U_p} \rangle}, \quad (5)$$

669 where $\overline{\alpha}_p$ and $\overline{\alpha}_o$ are the simulated and observed time-averaged wind direc-
 670 tions, respectively. The brackets indicate averaging over the probes locations.
 671 A perfect model would result in $SAA = 0$.

672 The skill scores for the pollutant concentrations presented in Eqs. 6–9 are
 673 among those recommended by Hanna et al. (1993) to quantitatively measure
 674 the performance of a pollutant dispersion model. They include the fractional
 675 bias (FB), the fraction of simulation results within a factor of two of the obser-
 676 vations ($FAC2$), the geometric mean bias (MG), and the geometric variance
 677 (VG):

$$678 \quad FB = \frac{\langle \overline{C}_p \rangle - \langle \overline{C}_o \rangle}{0.5(\langle \overline{C}_p \rangle + \langle \overline{C}_o \rangle)}, \quad (6)$$

$$679 \quad FAC2 = \frac{1}{N_t} \sum_{i=1}^{N_t} N_i \text{ with } N_i = \begin{cases} 1 & \text{if } \frac{1}{2} \leq \frac{\overline{C}_{pi}}{\overline{C}_{oi}} \leq 2 \\ 0 & \text{else} \end{cases}, \quad (7)$$

$$680 \quad MG = \exp(\langle \ln(\overline{C}_p) \rangle - \langle \ln(\overline{C}_o) \rangle), \quad (8)$$

$$681 \quad VG = \exp[\langle (\ln(\overline{C}_o) - \ln(\overline{C}_p))^2 \rangle], \quad (9)$$

682 where \overline{C}_o and \overline{C}_p are the time-averaged observations and model simulation
 683 results, respectively. Chang and Hanna (2004) give the following values for an
 684 acceptable model performance:

$$FAC2 > 0.5, \quad -0.3 < FB < 0.3, \quad 0.7 < MG < 1.3, \quad VG < 1.6,$$

685 where $FAC2$, MG , and FB measure the systematic bias of the model results
 686 and indicate only the systematics errors, whereas VG measures the mean rela-
 687 tive scatter of the data and accounts for both systematic and random errors.
 688 In order to reduce the influence of extremely low pollutant concentration val-
 689 ues on MG and VG , the instrument threshold (0.04 ppm for the PIDs and
 690 0.01 ppm for the UVIDs) is used as lower bound for C_o and C_p . The value of
 691 $FAC2$ is not sensitive to the variable distribution and is the most robust skill
 692 score according to Chang and Hanna (2004).

693 In contrast to Hanna et al. (1993) and Chang and Hanna (2004), the metrics
 694 FB and MG are here defined as the difference between model result and the
 695 observation. Therefore, FB (respectively MG) is positive (respectively above 1)
 696 when the model overestimates the pollutant concentrations; this corresponds
 697 to the standard definition of a model bias.

698 A graphic representation of the skill scores for the CFD40 (dashed bars),
 699 the CFD3000 (dotted bars), and the multiscale (crossed bars) configurations
 700 is given in Fig. 13. For the wind speed and the wind direction, the scores
 701 are calculated for the 27 probes available for that pollutant release among
 702 the sonic probes displayed in Fig. 2. A distinction is made between probes
 703 outside (in red) and within (in green) the container array. The probes outside
 704 the container array might be located upstream, above, or downstream of the
 705 containers. They are mounted on mast T, towers N, S and at the top level
 706 of towers A, B, and D. The probes within the container array are close to

706 the ground (UU, V, LANL2D, bottom level of towers A, B, and D). For the
707 pollutant concentration, a distinction is made between horizontal (on lines 1 to
708 4) and vertical probes (mounted on mast T, towers A, B, and D). The scores
709 for the horizontal and the vertical probes are shown in cyan and magenta,
710 respectively. For each skill score, the result for all probes is shown in blue.

711 6.2 Wind Speed and Wind Direction

712 The hit rate for the wind speed is shown on Fig. 13a. Outside of the container
713 array, CFD3000 and MSC present a perfect score of $HR = 1$, whereas the
714 CFD40 has $HR = 0.92$. This is most probably because the CFD40 configura-
715 tion has a model top at $z = 40$ m, which leads to an artificial overestimation
716 of the wind speed above the containers, especially in the upper part of the do-
717 main (Fig. 9). Because the CFD-like configuration follows Franke et al. (2011)
718 recommendations, this artificial wind speed overestimation is minimized and
719 the hit rate remains satisfactory.

720 Inside the array, CFD40 presents $HR = 0.57$. This score is improved with
721 CFD3000 where $HR = 0.71$. For the MSC, $HR = 0.79$ inside the array. These
722 results show that a low top boundary affects the flow inside the array in a non-
723 negligible way for the CFD-like configurations. Furthermore, accounting for the
724 large-scale turbulent fluctuations enhances wind speed simulation within the
725 container array. As a consequence, the hit rate for all probes is also improved
726 using the MSC (0.74 for CFD40, 0.85 for CFD3000 and 0.89 for MSC).

727 For the wind direction outside of the container array, the SAA is rather
728 satisfactory with similar values of 7.44, 7.92 and 7.92 for CFD40, CFD3000,
729 and MSC, respectively. Contrary to the wind speed, the wind direction simu-
730 lation, at least outside of the container array, is not improved with the MSC.
731 Inside the container array, the SAA score is very poor for all configurations:
732 64, 62.92, and 62.12 for CFD40, CFD3000, and MSC, respectively. The slight
733 improvement for MSC is negligible. Two points might reduce the importance
734 of this bad score. First, the wind direction is varying quite rapidly over short
735 distances. In these conditions, the wind direction simulations within the con-
736 tainer array are expected to be difficult and not very accurate. Second, the
737 probes available inside the array are not very representative. Indeed, as can
738 be seen on Fig. 2, they are mostly located in two specific areas: in the recircu-
739 lation cell of container L4 (UU and LANL2D probes) and around mast T (V
740 probes). Despite these points, it is clear that, for all configurations, the model
741 does not simulate correctly the overall wind direction in the container array.
742 This could also be another reason for the difficulties encountered by the model
743 in getting the plume deflection correct as shown in Fig. 10.

744 6.3 Pollutant Concentration

745 For the two CFD-like configurations, Fig. 13c shows that $FAC2 = 0.73$, 0.50,
746 and 0.65 for the horizontal, the vertical, and all probes, respectively. This

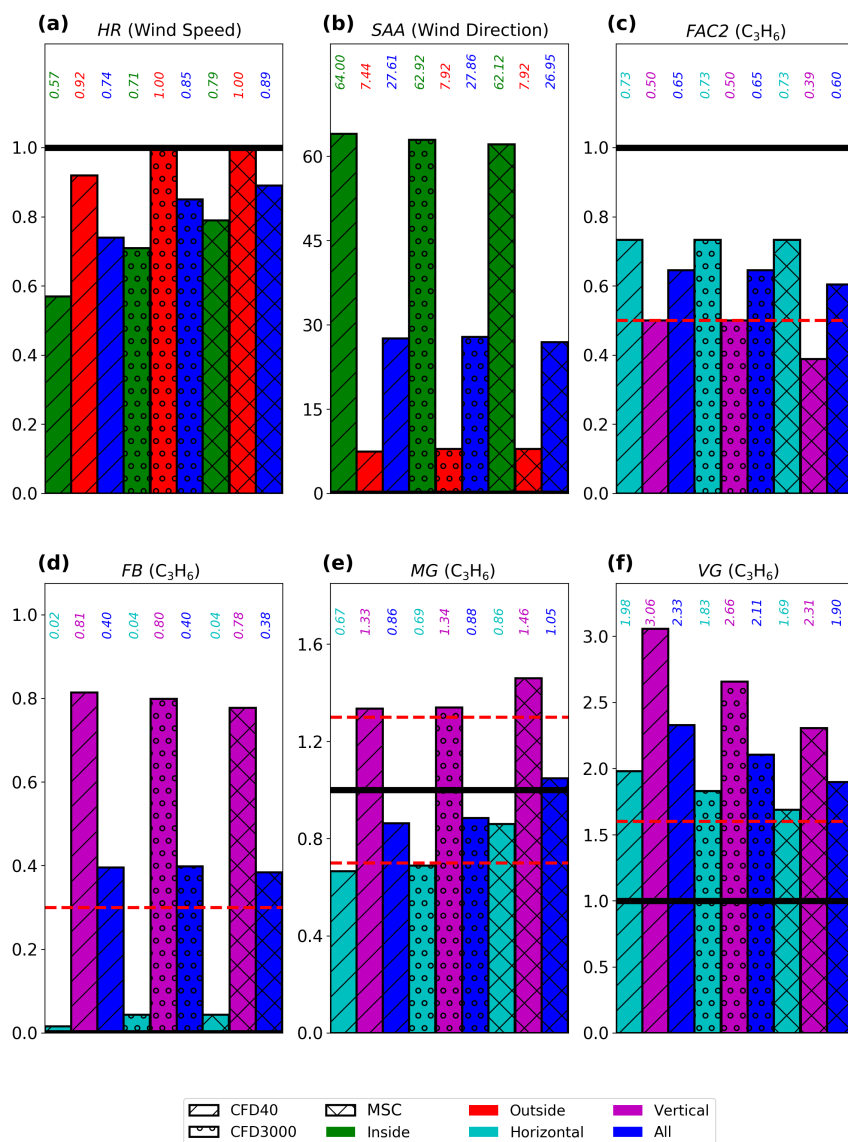


Fig. 13 Skill scores for the wind speed and the pollutant concentration for the CFD-like and MSC configurations. The thick horizontal black line indicates a perfect skill score. The dashed red lines indicate an acceptable skill score according to Chang and Hanna (2004)

747 is very satisfactory as the score for each probes ensemble is above or equal
 748 to the acceptable model performance threshold value of 0.5. The skill scores
 749 calculated in the present study cannot be compared with those from the lit-

750 erature (Milliez and Carissimo 2007) as the latter are obtained for a 200-s
751 nearly-stationary period filtering the large-scale turbulent fluctuations. The
752 horizontal FB value is also very satisfactory with a value of 0.02 for CFD40
753 and 0.04 for CFD3000. However, the vertical FB values of 0.80 and 0.81 show
754 that the CFD-like configurations strongly overestimate the concentration for
755 the vertical probes. This overestimation is also found by looking at the value
756 of MG (≈ 1.3) and at the vertical concentration profiles for Mast T and Tower
757 B displayed in Fig. 12.

758 The MSC gives $FAC2 = 0.73$ for the horizontal probes. This good score is
759 identical to the CFD-like configuration. The score drops to 0.39 for the vertical
760 probes, which is below the acceptable value threshold. The total $FAC2$ value
761 of 0.6 is satisfactory. The horizontal FB value is very close to the ideal value of
762 0. However, as for the CFD-like configurations, the vertical FB value of 0.79
763 shows that the MSC overestimates the concentration for the vertical probes.
764 Similarly to the CFD-like configurations, this overestimation is confirmed by
765 the value of MG (1.46) and by the vertical profiles displayed in Fig. 12.

766 The value of $FAC2$ does not show any improvement with the MSC. The
767 score is worse for the vertical probes (0.39 versus 0.50 for the CFD-like con-
768 figurations). These results are surprising because the pollutant concentration
769 profiles presented in Figs. 11 and 12 show a slight but clear improvement with
770 the MSC. The reason is simple: the multiscale and the CFD-like configurations
771 present mostly differences where both are within or outside a factor of two of
772 the observations, making impossible for the $FAC2$ parameter to distinguish
773 which configuration is the best. A thorough analysis can be performed using
774 the other metrics. For the horizontal probes, the MSC gives $MG = 0.86$, which
775 is within the acceptable model range from Chang and Hanna (2004). This is
776 not the case for the CFD-like configurations where $MG < 0.7$. A similar re-
777 sult is found for VG (1.69 versus 1.83 for CFD3000 and 1.98 for CFD40).
778 The metrics MG and VG are sensitive to low pollutant concentration values,
779 which can be found for probes close to the edge of the plume. In other terms,
780 the experimental low pollutant concentrations are more accurately captured
781 with the MSC than with the CFD-like ones, a result in agreement with the
782 horizontal transects presented in Fig. 11.

783 Concerning the vertical probes, the probes at the bottom of tower B are
784 within the $FAC2$ range for the CFD-like configurations but not for the mul-
785 tiscale one. For the probes at mast T (respectively tower D), the multiscale
786 results are overall better than the CFD-like ones but the CFD-like results re-
787 main inside (respectively outside) the $FAC2$ range of the experimental values.
788 As a result, the vertical $FAC2$ is better for the CFD-like configurations, even
789 though other metrics (FB , VG) indicate that these configurations overesti-
790 mate the vertical concentration more than the MSC. Overall, this example
791 is a good reminder that it is safer to evaluate the model performance using
792 several complementary metrics.

793 6.4 Influence of the Top Boundary Height for the CFD-like Configurations.

794 The CFD40 configuration has a low top boundary, as it is usually done in CFD.
795 Even if this configuration respects the literature recommendations (Franke
796 et al. 2011; Blocken 2015), this is not without consequences on the wind speed
797 estimation. There is a small Venturi effect above the container array and the
798 CFD3000 wind speed results are in better agreement with the observations
799 than the CFD40 ones. This statement is true outside and inside the container
800 array. However, no such conclusions can be drawn for the pollutant dispersion.
801 The horizontal and vertical profiles such as most of the skill score estimators
802 do not show a significant improvement in the pollutant dispersion simulation
803 with the CFD3000 case. The model improvement is more significant, even if
804 it remains slight, with the MSC. The pollutant dispersion results presented
805 here are therefore more dependent on the large-scale turbulent structures of
806 the ABL than of the top height of the domain boundary.

807 6.5 Plume Deflection Underestimation Impact on the Model Performance

808 The overall weaker model performance for the vertical probes can mostly be
809 explained by the plume deflection underestimation and to a lesser extent by
810 the vertical profiles sensitivity to the plume direction. The plume deflection
811 underestimation has important consequences on the results accuracy as it is
812 most probably responsible of the concentration overestimation at tower B.
813 Indeed, tower B is located at the left edge of the plume (from a wind flow
814 point of view, see Figs. 2 and 10) in the experiment but closer to the plume
815 centreline in the presented numerical results. This phenomenon impacts the
816 results accuracy in all configurations. The pollutant underestimation at tower
817 D, located at the edge of the plume, is another consequence of the plume
818 deflection underestimation.

819 The consequences of the plume deflection underestimation are also more
820 important for the vertical profiles because they are sensitive to the plume direc-
821 tion (Milliez and Carissimo 2007). Indeed, if one or several profiles are located
822 at the edge of the plume (as tower B and D in the present case), where the
823 pollutant concentrations are low (and therefore difficult to simulate), a small
824 imprecision in the plume direction impacts the simulated concentration. For
825 the present study, few observed vertical profiles are available, which amplifies
826 the impact of one single profile on the total skill score.

827 6.6 Pollutant Dispersion

828 The results presented in Sect. 5 show that the pollutant dispersion is under-
829 estimated. This flaw is found for all configurations but is more important for
830 the CFD-like ones. The reason for this deficiency is not the advection scheme.
831 First, because WENO5 is known to be a diffusive numerical scheme. Second,

832 because this drawback has been found regardless of the advection scheme
833 (WENO5 or CEN4TH, not shown here). Like for the pollutant plume deflec-
834 tion underestimation, the dispersion underestimation is probably due to the
835 difficulties of the model to simulate the wind direction in the array and to the
836 strong jets rushing between the containers (Fig. 10).

837 6.7 Conclusion

838 The overall performance metrics show that performing a LES simulation of the
839 MUST case using a MSC rather than a CFD-like one only slightly improves
840 the pollutant concentration results. Accounting for the large ABL turbulent
841 structures is therefore improving the numerical results accuracy for the pol-
842 lutant dispersion but significantly less than what is reported in Wiersema
843 et al. (2020) for the JU2003 field campaign in Oklahoma City. The main dif-
844 ferences between both cases are the horizontal and vertical size distribution
845 of the buildings. The MUST case presents an array of containers with uni-
846 form height, regular shape, and spacing, whereas downtown Oklahoma City
847 presents important variations in buildings horizontal and vertical size, shape,
848 and spacing. The present results show that the benefit of accounting for the
849 large-scale ABL structures to simulate the pollutant dispersion in a city is de-
850 pendent on the city specific configuration. In the MUST case, which represents
851 an idealized city, this benefit is limited whereas, according to Wiersema et al.
852 (2020), it is very important for JU2003.

853 7 Summary and Conclusion

854 In the present study, LESs are performed with the mesoscale atmospheric
855 model Meso-NH to investigate the influence of the ABL turbulence on the
856 mean flow, the turbulence, and the pollutant dispersion in the MUST ideal-
857 ized urban-like environment. The influence of a limited vertical model domain
858 extent, which is usually used in CFD simulations, is also investigated. Three
859 configurations are studied: two CFD-like configurations, with and without lim-
860 ited vertical extent, composed of a single high-resolution model domain where
861 a steady velocity profile is imposed at the domain boundaries and a multiscale
862 configuration, composed of four grid-nested domains with increasing horizon-
863 tal resolution. Only the MSC accounts for all scales of atmospheric turbulence
864 prevailing in the ABL. The building-like obstacles are represented using the
865 IBM.

866 A new turbulence recycling method is successfully used to enhance the
867 turbulence scale transition between two nested subdomains: the prognostic
868 variable fluctuations from a vertical plane parallel to the inflow boundary
869 are calculated with respect to a moving temporal average and added to the
870 prognostic variable field at the inlet.

871 The wind characteristics such as the wind speed, the wind direction, and
872 the TKE upstream of the container array are well reproduced with the MSC,

873 showing the efficiency of the turbulence downscaling from the meso-scale to
874 the microscale as well as of the turbulence recycling method. Furthermore,
875 contrary to the CFD-like configurations, the MSC is able to reproduce the
876 mesoscale turbulent structures crossing the container array, allowing further
877 investigation of their impact on the pollutant dispersion.

878 The accuracy of the numerical results is evaluated with various skill scores,
879 including those recommended by Chang and Hanna (2004) for the pollutant
880 concentration. The CFD-like configuration with a limited domain height tends
881 to overestimate the wind speed, due to a small Venturi effect above the con-
882 tainer array. This is not the case for the CFD-like configuration extending over
883 the entire ABL. The MSC results are the ones in better agreement with the
884 experimental measurements of Yee and Biltoft (2004) for the wind speed. All
885 configurations show an equivalent good performance for the wind direction
886 outside the container array but fail to simulate accurately the wind direction
887 inside the array. Concerning the pollutant concentration, the two CFD-like
888 configurations are almost identical, confirming that there is no need to solve
889 the entire ABL in such configuration. The MSC presents only a slight im-
890 provement in terms of pollutant dispersion simulation. Overall, the present
891 study shows that the microscale numerical simulation of wind speed and pol-
892 lutant dispersion in an urban environment benefits from taking into account
893 the ABL turbulence. However, this benefit is significantly less important than
894 the one described by Wiersema et al. (2020) with the WRF model on the
895 JU2003 field campaign in Oklahoma City. The MUST idealized city config-
896 uration overcomes the effects of a specific urban environment on the results.
897 The present work shows that the general conclusion of Wiersema et al. (2020)
898 can be verified in an idealized case. However, it also highlights that the spe-
899 cific configuration of the city seems to have a strong impact on the benefit
900 of accounting for large ABL turbulent structures. For the MUST case, where
901 obstacles have an uniform height, size, shape, and spacing, the benefit is lim-
902 ited. For the JU2003 case, where the buildings present important variations in
903 buildings height, size, shape, and spacing, the benefit is important (Wiersema
904 et al. 2020). It is also possible that idealized models using generic buildings like
905 MUST or in Cheng and Castro (2002) are too simple to properly represent the
906 complex phenomena that drive pollutant transport in real cities. In that case,
907 the influence of parameters such as the presence of tall buildings, non-regular
908 horizontal dimensions or spacing of the obstacles and their link with the ABL
909 turbulence and pollutant dispersion simulation should be investigated by per-
910 forming a study similar to the present work on a field experiment dataset
911 where obstacles have different shape, height, and spacing, like Jack Rabbit II
912 (Pirhalla et al. 2020; Mazzola et al. 2021).

913 In addition, it is worth mentioning that the present results are limited to a
914 near-neutral case. For non-neutral atmospheric conditions, the ABL turbulence
915 may have a different impact on the microscale structures of the urban canopy.
916 This should be investigated in future studies, including the full radiative effects
917 in the canopy.

918 This study also confirms that the IBM is a promising way to represent the
919 flow interaction with buildings in atmospheric models for urban applications.
920 But it also shows that the MNH-IBM model presents room for improvement.
921 The most obvious flaw of the model is the plume deflection underestimation.
922 A sensitivity study to the wall roughness or the law of the wall should be
923 undertaken to better understand this flaw. This drawback directly impacts
924 the pollutant dispersion simulation accuracy as it reduces the plume spreading
925 compared with the observations, at least close to the pollutant release location.

926 More broadly, high-resolution numerical simulations of urban areas using
927 the IBM appear as a suitable tool to calculate parameters such as cities drag
928 coefficient to improve parametrizations in mesoscale atmospheric simulations.

929 **Acknowledgements** We are grateful to the three anonymous reviewers for their in-depth
930 review and their constructive comments. We would like to thank the Defense Threat Reduc-
931 tion Agency (DTRA) for providing access to the MUST data. We would like to thank
932 Mélanie Rochoux, Laëticia Thouron, Antoine Verrelle and Franck Auguste for the helpful
933 discussions so as Quentin Rodier and Juan Escobar for their precious help with Meso-NH.
934 Tim Nagel’s postdoctoral position was funded by the FCS-STAE foundation and the IRT
935 Saint-Exupéry, Toulouse, under the PPM project and by the EU LIFE climate change adap-
936 tation 2018 project Generate REsiliENt actions agaiNst the HEat islAnd effect on uRban
937 Territory (Green Heart; LIFE18 CCA/FR/001150).

938 References

- 939 Allwine K, Leach M, Stockham L, Shinn J, Hosker R, Bowers J, Pace J (2004)
940 J7. 1 Overview of Joint Urban 2003—an atmospheric dispersion study in
941 Oklahoma City
- 942 Allwine KJ, Flaherty JE (2006) Joint Urban 2003: Study overview and in-
943 strument locations. Pacific Northwest National Lab.(PNNL), Richland, WA
944 (United States), Tech rep
- 945 Auguste F, Réa G, Paoli R, Lac C, Masson V, Cariolle D (2019) Implementa-
946 tion of an immersed boundary method in the Meso-NH v5.2 model: applica-
947 tions to an idealized urban environment. *Geosci Model Dev* 12(6):2607–2633
- 948 Auguste F, Lac C, Masson V, Cariolle D (2020) Large-eddy simulations with
949 an immersed boundary method: Pollutant dispersion over urban terrain.
950 *Atmosphere* 113(11):200–200
- 951 Biltoft CA (2001) Customer report for mock urban setting test. DPG Docu-
952 ment Number 8-CO-160-000-052. Prepared for the Defence Threat Reduc-
953 tion Agency, Tech rep
- 954 Blocken B (2015) Computational Fluid Dynamics for urban physics: Impor-
955 tance, scales, possibilities, limitations and ten tips and tricks towards accu-
956 rate and reliable simulations. *Build Environ* 91:219–245
- 957 Calhoun R, Gouveia F, Shinn J, Chan S, Stevens D, Lee R, Leone J (2004)
958 Flow around a complex building: Comparisons between experiments and a
959 Reynolds-averaged Navier–Stokes approach. *J Appl Meteorol* 43(5):696–710
- 960 Chang JC, Hanna SR (2004) Air quality model performance evaluation. *Me-
961 teorol Atmos Phys* 87(1-3):167–196

- 962 Cheng H, Castro IP (2002) Near wall flow over urban-like roughness.
963 *Boundary-Layer Meteorol* 104(2):229–259
- 964 Colella P, Woodward PR (1984) The piecewise parabolic method (ppm) for
965 gas-dynamical simulations. *J Comput Phys* 54(1):174–201
- 966 Couvreur F, Bazile E, Rodier Q, Maronga B, Matheou G, Chinita MJ, Ed-
967 wards J, van Stratum BJ, van Heerwaarden CC, Huang J, et al. (2020)
968 Intercomparison of large-eddy simulations of the antarctic boundary layer
969 for very stable stratification. *Boundary-Layer Meteorol* 176(3):369–400
- 970 Cox R, Bauer BL, Smith T (1998) A mesoscale model intercomparison. *Bull*
971 *Am Meteorol Soc* 79(2):265–284
- 972 Cuxart J, Bougeault P, Redelsperger JL (2000) A turbulence scheme allowing
973 for mesoscale and large-eddy simulations. *Q J R Meteorol Soc* 126(562):1–30
- 974 Dauxois T, Peacock T, Bauer P, Caulfield C, Cenedese C, Gorié C, Haller G,
975 Ivey G, Linden P, Meiburg E, et al. (2021) Confronting grand challenges in
976 environmental fluid mechanics. *Phys Rev Fluid* 6(2):020,501
- 977 Dejoan A, Santiago J, Martilli A, Martin F, Pinelli A (2010) Comparison
978 between large-eddy simulation and Reynolds-averaged Navier–Stokes com-
979 putations for the must field experiment. Part II: effects of incident wind
980 angle deviation on the mean flow and plume dispersion. *Boundary-Layer*
981 *Meteorol* 135(1):133–150
- 982 Durran DR (1989) Improving the anelastic approximation. *J Atmos Sci*
983 46(11):1453–1461
- 984 Franke J, Hellsten A, Schlunzen KH, Carissimo B (2011) The cost 732 best
985 practice guideline for cfd simulation of flow in the urban environment: a
986 summary. *Int J Environ Pollut* 44(1-4):419–427
- 987 Gal-Chen T, Somerville RC (1975) On the use of a coordinate transformation
988 for the solution of the Navier–Stokes equations. *J Comput Phys* 17(2):209–
989 228
- 990 García-Sánchez C, Gorié C (2018) Uncertainty quantification for microscale
991 CFD simulations based on input from mesoscale codes. *J Wind Eng Ind*
992 *Aerodyn* 176:87–97
- 993 García-Sánchez C, van Beeck J, Gorié C (2018) Predictive large eddy simu-
994 lations for urban flows: Challenges and opportunities. *Build Environ* 139:146–
995 156
- 996 Hanna S, Chang J, Strimaitis D (1993) Hazardous gas model evaluation with
997 field observations. *Atmos Environ A, Gen Top* 27(15):2265–2285
- 998 Honnert R, Masson V, Lac C, Nagel T (2021) A theoretical analysis of mixing
999 length for atmospheric models from micro to large scales. *Front Earth Sci*
1000 8:582,056
- 1001 Iaccarino G, Verzicco R (2003) Immersed boundary technique for turbulent
1002 flow simulations. *Appl Mech Rev* 56(3):331–347
- 1003 Jabouille P, Guivarch R, Kloos P, Gazen D, Gicquel N, Giraud L, Asencio N,
1004 Ducrocq V, Escobar J, Redelsperger JL, et al. (1999) Parallelization of the
1005 french meteorological mesoscale model Méso-NH. In: *European Conference*
1006 *on Parallel Processing*, Springer, pp 1417–1422

- 1007 Kataoka H, Mizuno M (2002) Numerical flow computation around aerolastic
1008 3D square cylinder using inflow turbulence. *Wind Struct Int J* 5(2/4):379–
1009 392
- 1010 Kim W, Choi H (2019) Immersed boundary methods for fluid-structure inter-
1011 action: A review. *Int J Heat Fluid Flow* 75:301–309
- 1012 Lac C, Chaboureau P, Masson V, Pinty P, Tulet P, Escobar J, Leriche M,
1013 Barthe C, Aouizerats B, Augros C, et al. (2018) Overview of the Meso-NH
1014 model version 5.4 and its applications. *Geosci Model Dev* 11:1929–1969
- 1015 Lin SJ, Rood RB (1996) Multidimensional flux-form semi-lagrangian transport
1016 schemes. *Mon Weather Rev* 124(9):2046–2070
- 1017 Lund TS, Xiohua W, Squires KD (1998) Generation of turbulent inflow
1018 data for spatially developing boundary layer simulations. *J Comput Phys*
1019 140(2):233–258
- 1020 Lundquist KA, Chow FK, Lundquist JK (2010) An immersed boundary
1021 method for the Weather Research and Forecasting model. *Mon Weather*
1022 *Rev* 138(3):796–817
- 1023 Lundquist KA, Chow FK, Lundquist JK (2012) An immersed boundary
1024 method enabling large-eddy simulations of flow over complex terrain in the
1025 WRF model. *Mon Weather Rev* 140(12):3936–3955
- 1026 Lunet T, Lac C, Auguste F, Visentin F, Masson V, Escobar J (2017) Combina-
1027 tion of WENO and explicit Runge–Kutta methods for wind transport in
1028 the Meso-NH model. *Mon Weather Rev* 145(9):3817–3838
- 1029 Maronga B, Gryscha M, Heinze R, Hoffmann F, Kanani-Sühring F, Keck M,
1030 Ketelsen K, Letzel MO, Sühring M, Raasch S (2015) The parallelized large-
1031 eddy simulation model (PALM) version 4.0 for atmospheric and oceanic
1032 flows: model formulation, recent developments, and future perspectives.
1033 *Geosci Model Dev* 2:2514–2551
- 1034 Masson V, Le Moigne P, Martin E, Faroux S, Alias A, Alkama R, Barbu
1035 A, Boone A, Bouysse F, et al. (2013) The SURFEXv7.2 land and ocean
1036 surface platform for coupled or offline simulation of earth surface variables
1037 and fluxes. *Geosci Model Dev* 6:929–960
- 1038 Mazzola T, Hanna S, Chang J, Bradley S, Meris R, Simpson S, Miner S, Gant
1039 S, Weil J, Harper M, et al. (2021) Results of comparisons of the predictions
1040 of 17 dense gas dispersion models with observations from the Jack Rabbit
1041 II chlorine field experiment. *Atmos Environ* 244:117,887
- 1042 Mesinger F, Arakawa A (1976) Numerical methods used in the atmospheric
1043 models
- 1044 Milliez M, Carissimo B (2007) Numerical simulations of pollutant dispersion in
1045 an idealized urban area, for different meteorological conditions. *Boundary-*
1046 *Layer Meteorol* 122(2):321–342
- 1047 Muñoz-Esparza D, Kosović B, Mirocha J, van Beeck J (2014) Bridging the
1048 transition from mesoscale to microscale turbulence in numerical weather
1049 prediction models. *Boundary-Layer Meteorol* 153(3):409–440
- 1050 Muñoz-Esparza D, Kosović B, van Beeck J, Mirocha J (2015) A stochastic
1051 perturbation method to generate inflow turbulence in large-eddy simulation
1052 models: Application to neutrally stratified atmospheric boundary layers.

- 1053 Phys Fluids 27(3)
- 1054 Park SB, Baik JI, Han BS (2015a) Large-eddy simulation of turbulent flow in
1055 a densely built-up urban area. *Environ Fluid Mech* 15(2):235–250
- 1056 Park SB, Baik JI, Lee SH (2015b) Impacts of mesoscale wind on turbulent
1057 flow and ventilation in a densely built-up urban area. *J Appl Meteorol Clim*
1058 54(4):811–824
- 1059 Pirhalla M, Heist D, Perry S, Hanna S, Mazzola T, Arya SP, Aneja V (2020)
1060 Urban wind field analysis from the Jack Rabbit II special sonic anemometer
1061 study. *Atmos Environ* 243:117,871
- 1062 Rochoux M, Thouron L, Rea G, Auguste F, Jaravel T, Vermorel O (2021)
1063 Large-eddy simulation multi-model comparison of the MUST trial 2681829.
1064 Technical report - tr-cmgc-21-72
- 1065 Roth M (2000) Review of atmospheric turbulence over cities. *Q J R Meteorol*
1066 *Soc* 126(564):941–990
- 1067 Skamarock WC (2004) Evaluating mesoscale NWP models using kinetic energy
1068 spectra. *Mon Weather Rev* 132(12):3019–3032
- 1069 Skamarock WC, Klemp JB, Dudhia J, Gill DO, Barker DM, Wang W, Powers
1070 JG (2008) A description of the advanced research WRF version 3. NCAR
1071 technical note-475+ str
- 1072 Stein J, Richard E, Lafore JP, Pinty J, Asencio N, Cosma S (2000) High-
1073 resolution non-hydrostatic simulations of flash-flood episodes with grid-
1074 nesting and ice-phase parameterization. *Meteorol Atmos Phys* 72(2-4):203–
1075 221
- 1076 Sussman M, Smereka P, Osher S (1994) A level set approach for computing
1077 solutions to incompressible two-phase flow
- 1078 Tominaga Y, Stathopoulos T (2013) CFD simulation of near-field pollutant
1079 dispersion in the urban environment: A review of current modeling tech-
1080 niques. *Atmos Environ* 79:716–730
- 1081 Tseng YH, Ferziger JH (2003) A ghost-cell immersed boundary method for
1082 flow in complex geometry. *J Comput Phys* 192(2):593–623
- 1083 Wiersema DJ, Lundquist KA, Chow FK (2020) Mesoscale to microscale sim-
1084 ulations over complex terrains with the immersed boundary method in the
1085 weather research and forecasting model. *Mon Weather Rev* 148(2):577–595
- 1086 Yang G, Causon D, Ingram D, Saunders R, P B (1997) A cartesian cut cell
1087 method for compressible flows. Part A: Static body problems. *Aeronaut J*
1088 101(1002):47–56
- 1089 Yee E, Biltoft CA (2004) Concentration fluctuation measurements in a plume
1090 dispersing through a regular array of obstacles. *Boundary-Layer Meteorol*
1091 111(3):363–415
- 1092 Zängl G, Gantner L, Hartjenstein G, Noppel H (2004) Numerical errors above
1093 steep topography: A model intercomparison. *Meteorol Z* 13(2):69–76